

Robust multi-mode superconducting qubit designed with evolutionary algorithms

P. García-Azorín,^{1,2,*} F. A. Cárdenas-López,³ G. B. P. Huber,^{4,5} G. Romero,⁶
M. Werninghaus,^{4,5} F. Motzoi,^{3,7} S. Filipp,^{4,5,8} and M. Sanz^{1,9,2,10,†}

¹*Department of Physical Chemistry, University of the Basque Country UPV/EHU, Apartado 644, 48080 Bilbao, Spain*

²*EHU Quantum Center, University of the Basque Country UPV/EHU, Apartado 644, 48080 Bilbao, Spain*

³*Forschungszentrum Jülich GmbH, Peter Grünberg Institute,
Quantum Control (PGI-8), 52425 Jülich, Germany*

⁴*Walther-Meißner-Institut, Bayerische Akademie der Wissenschaften, 85748 Garching, Germany*

⁵*Technical University of Munich, TUM School of Natural Sciences,
Department of Physics, Garching 85748, Germany*

⁶*Departamento de Física, CEDENNA, Universidad de Santiago de Chile,
Avenida Víctor Jara 3493, 9170124, Santiago, Chile*

⁷*Institute for Theoretical Physics, University of Cologne, 50937 Cologne, Germany*

⁸*Munich Center for Quantum Science and Technology (MCQST),
Schellingstraße 4, 80799 München, Germany*

⁹*Basque Center for Applied Mathematics (BCAM),
Alameda de Mazarredo, 14, 48009 Bilbao, Spain*

¹⁰*IKERBASQUE, Basque Foundation for Science, Plaza Euskadi 5, 48009, Bilbao, Spain*

(Dated: July 29, 2024)

Multi-mode superconducting circuits offer a promising platform for engineering robust systems for quantum computation. Previous studies have shown that single-mode devices cannot simultaneously exhibit resilience against multiple decoherence sources due to conflicting protection requirements. In contrast, multi-mode systems offer increased flexibility and have proven capable of overcoming these fundamental limitations. Nevertheless, exploring multi-mode architectures is computationally demanding due to the exponential scaling of the Hilbert space dimension. Here, we present a multi-mode device designed using evolutionary optimization techniques, which have been shown to be effective for this computational task. The proposed device was optimized to feature an anharmonicity of a third of the qubit frequency and reduced energy dispersion caused by charge and magnetic flux fluctuations. It exhibits improvements over the fundamental errors limiting Transmon and Fluxonium coherence and manipulation, aiming for a balance between low depolarization error and fast manipulation; furthermore demonstrating robustness against fabrication errors, a major limitation in many proposed multi-mode devices. Overall, by striking a balance between coupling matrix elements and noise protection, we propose a device that paves the way towards finding proper characteristics for the construction of superconducting quantum processors.

I. INTRODUCTION

Among the various platforms for realizing quantum information processing, superconducting qubits have emerged as one of the leading contenders due to their scalability, controllability, and compatibility with existing semiconductor fabrication techniques. However, the widespread adoption of superconducting qubits for practical quantum computation faces significant challenges, primarily stemming from its scalability and limited coherence times.

Since the first proposals of superconducting systems to perform quantum computation, the capa-

bilities and computational power have been limited by decoherence. Errors affecting superconducting devices have been traditionally classified into two main categories: errors producing dephasing and errors producing depolarization. In the development of the first superconducting qubits, starting from the Cooper-Pair Box [1, 2] and Flux qubit [3], dephasing was the limiting factor constraining operability due to the large sensitivity to environmental fluctuations. To overcome the initial limitations, superconducting systems were engineered to suppress specific noise vulnerabilities, a good example of that being the Transmon device [4], expressing a highly suppressed sensitivity to external charge bias. Despite this improvement, the Transmon still suffers some limitations, mainly stemming from the large dipole matrix elements that lead to a strong dissipation and induce

* pablo.garciaa@ehu.eus

† mikel.sanz@ehu.es

depolarization. As an alternative to suppress this depolarization effect, the Fluxonium device was proposed [5], where the charge matrix elements present reduced values, at the cost of a reasonable dephasing error. By relying on the reduced amplitude of external magnetic flux fluctuations compared to charge fluctuations, coherence times were improved, which led to a significant improvement in coherence times [6–8], and thus, computational power. However, on top of these limitations, the necessity of operation requires the system to present large anharmonicities and large charge (flux) matrix elements, in order to be able to apply fast gate operations. This further imposes another tradeoff among matrix elements, anharmonicities and coherence times. Consequently, the presence of fundamentally different error sources requires specific system characteristics, which can, in certain scenarios, conflict, making the construction of fully robust systems difficult to achieve [9].

Most of the devices mentioned above rely on a single degree of freedom to encode the quantum information, that is, one single mode, which can be physically understood as the number of Cooper pairs contained on an island of superconducting material, the superconducting phase difference between two of them or even a persistent current oscillating in a superconducting loop. In recent years, the difficulties in finding proper tradeoffs for single-mode devices have motivated the development of more complex circuits, with an increasing number of elements constituting multi-mode systems [10]. Most of the multimode device proposals made so far rely on the construction of a protected subspace [11–13], based on symmetry [14] or parity protection [15, 16], intending to preserve the quantum state encoded against relaxation and dephasing. However, this still imposes significant challenges for manipulation, raising the necessity of operations that take the system out of the protection state and that still lead to decoherence [9, 14]. A different approach are multimode architectures without fundamental full state protection, but with improved tradeoffs between noise protection and controllability [17, 18]. Nevertheless, the design of systems with an increasing number of elements carries major difficulties. Not only the complexity in the exploration of the configuration space dramatically scales with the number of free parameters, but also the analysis of the properties of each configuration scales exponentially with the number of modes. This fact, summed to the difficulties in making a physical intuition of these complex systems, makes the engineering and optimization of multi-mode configurations a challenging task.

In this article, we present a multi-mode device, the

Diffuxmon, optimized to present suitable characteristics to perform quantum computation. The system was derived using computer-aided optimization techniques, in the form of evolutionary algorithms, based on the techniques developed in [19], to efficiently explore the large parameter space, aiming to minimize the number of iterations and computational power needed. The system was optimized to present a large anharmonicity ($\alpha \approx 2\pi \times 750$ MHz) at a reasonable qubit frequency ($\omega_{10} = 2\pi \times 2.5$ GHz), and balanced driving operator matrix elements ($|\langle 1|\hat{n}|0\rangle| \approx 0.4$). Transition rules were designed to overcome the most common leakage channels, canceling the $|1\rangle \rightarrow |2\rangle$ transition. The reduction of energy dispersion due to external charge and flux effects was targeted, with the goal of increasing dephasing times. By finding proper matrix element values, allowing for the implementation of fast operations while maintaining depolarization protection, accompanied by increased dephasing times, qubit frequency, and anharmonicity, we generated a system with improved gate time compared with the total coherence time.

The article is organized as follows. We start by presenting the multi-mode architecture, Sec. II. We discuss its fundamental characteristics, including spectral properties, transition rules, and sensitivity to external effects. In Sec. III, based on the characteristics discussed, we present some coherence times estimations, and comparisons with the two most extended superconducting qubits: Transmon and Fluxonium. After that we follow by presenting some single-qubit gate simulations in Sec. IV, and we present an active readout and reset mechanism for this device in Sec. V. For completeness, in Sec. VI we perform simulations regarding fabrication errors, and we study its robustness under parameter deviations, furthermore showing the feasibility of the capacitive relations considered for their match in 2D lithographic designs (Appendix C). Lastly, we discuss existing problems towards scalability VII, and we present a summary and conclusions in Sec. VIII.

II. SUPERCONDUCTING CIRCUIT

The circuit consists of four superconducting islands, three of them connected in series by two linear inductors and one Josephson junction, forming a loop. The remaining island is connected to the loop through a Josephson junction, forming a three-mode device. Additionally, it presents capacitive connections between every island in the circuit. The lumped-element schematic of the system is shown in Fig. 1(a), although some capacitive connections are

omitted for clarity. The circuit parameters considered are shown in Table I. The system was derived from the optimization of a general four superconducting islands structure (see Appendix D), considering capacitive connections between every island, to mimic the realistic capacitive relations in 2D lithographic designs (see Appendix C), and either a linear or non-linear inductor connection.

A. Hamiltonian

The Hamiltonian modeling the device, in terms of node variables (see Appendix A), is given by

$$\begin{aligned} \hat{H} = & 4\mathbf{n}^T \mathbf{E}_C \mathbf{n} + \frac{1}{2} \boldsymbol{\varphi}^T \mathbf{E}_L \boldsymbol{\varphi} \\ & - E_J^{b_0} \cos(\hat{\varphi}_1) - E_J^{b_5} \cos(\hat{\varphi}_2 - \hat{\varphi}_3) \\ & + \hat{H}_{\text{ext}}(n_{g_{\text{ext}}}, \varphi_{\text{ext}}), \end{aligned} \quad (1)$$

where $\mathbf{n} = (\hat{n}_1, \hat{n}_2, \hat{n}_3)^T$ and $\boldsymbol{\varphi} = (\hat{\varphi}_1, \hat{\varphi}_2, \hat{\varphi}_3)^T$ are the charge and phase vectors, with $\hat{n}_i = \hat{q}_i/(2e)$ and $\hat{\varphi}_i = (2\pi/\Phi_0)\Phi_i$, being \hat{q}_i and $\hat{\Phi}_i$ the charge and flux operators of node i respectively; $[E_C]_{ij} = (e^2/2)[C^{-1}]_{ij}$ and

Circuit parameters			
Branch	C (fF)	L (nH)	$E_J/(2\pi)$ (GHz)
b_0	11.62	–	2.5
b_1	12.48	–	–
b_2	15.31	35.21	–
b_3	12.29	–	–
b_4	10.27	32.82	–
b_5	10.94	–	6.85

Table I: Circuit parameter of the device depicted in Fig. 1(a).

$[E_L]_{ij} = (\Phi_0/2\pi)^2 [L^{-1}]_{ij}$ represent the matrices of charging and inductive energies respectively, with Φ_0 being the flux quantum and e the electron charge; we set node N_0 as the reference; and \hat{H}_{ext} models the effect of external charge and flux bias. From the circuit, we observe a quantum system of three modes, one *charge-like* $\{N_2\}$ and two *flux-like* $\{N_1, N_3\}$, strongly coupled together. The system is subjected to contributions from external charge bias $n_{g_{\text{ext}}}$ and external magnetic flux bias φ_{ext} , modeled by \hat{H}_{ext} . Their effect will be studied later in the article IID.

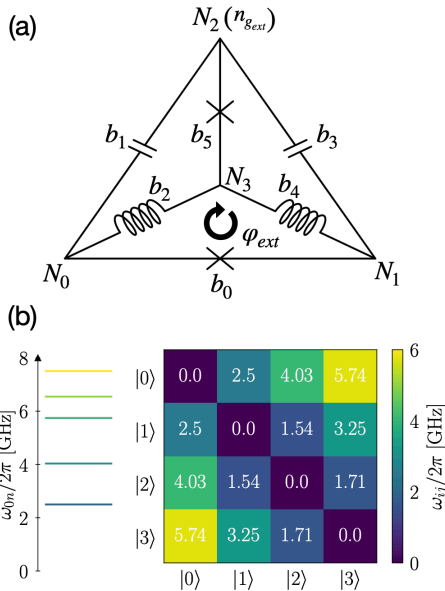


Figure 1: (a) Optimal lumped-element design consisting of four nodes $\mathcal{N} = \{N_0, N_1, N_2, N_3\}$, and five branches $\mathcal{B} = \{b_0, b_1, b_2, b_3, b_4\}$. (b) The global energy spectrum of the system for all three modes at $\varphi_{\text{ext}} = \pi$, where each element of the matrix on the right represents the energy difference between states $|i\rangle$ and $|j\rangle$.

B. Energy Spectrum

The numerically computed (see appendix B) energy spectrum of the device at the operation point $\varphi_{\text{ext}} = \pi$ is shown in fig. 1(b). We observe a highly anharmonic energy spectrum; the computational states present a frequency difference $\omega_{10} = 2\pi \times 2.5$ GHz, above thermal frequency assuming operation temperatures of 15 – 20 mK (~ 0.4 GHz). It presents an anharmonicity $\eta = \omega_2 - 2\omega_1 = 2\pi \times 1$ GHz with respect to the $|1\rangle \leftrightarrow |2\rangle$ transition. However, this leakage channel is further suppressed due to the matrix elements cancellation connecting $|1\rangle$ and $|2\rangle$ states ($|\langle 2|\hat{n}|1\rangle| \approx 0$) (see section IIC for the detailed discussion). Instead, the main leakage channel corresponds to the $|1\rangle \leftrightarrow |3\rangle$ transition that has a positive anharmonicity $\alpha = \omega_3 - 2\omega_1 = 2\pi \times 750$ MHz.

C. Matrix Elements

The matrix elements of charge and flux node operators dictate the coupling strength between the

electronic environment and the control lines for performing operations on the device, so decreasing the coupling strength intuitively increases the coherence time. However, at the same time, high isolation from the electronic can make the system uncontrollable and difficult to measure. For that reason, it is necessary to design devices with a balance between noise protection and control. The node charge and flux matrix elements of the device are shown in figure 2(a) (see Appendix B for details about the implementation of the different operators).

Focusing on the local charge matrix elements, if we select node N_1 as our coupling point for driving purposes, we observe a decrease of over a factor of 2 from the usual charge matrix element values in Transmon devices ($|\langle \hat{n} \rangle| \sim 1$) [4]. Despite this reduction, the values are still sufficiently large for external driving through a capacitively coupled voltage line (see Sec. IV), overcoming the manip-

ulability problems produced from the strong reduction of charge matrix elements in devices such as Fluxoniums ($|\langle \hat{n} \rangle| \sim 0.1$) [27, 38], Heavy Fluxoniums ($|\langle \hat{n} \rangle| \sim 0.01$) [37] or parity protected devices [15, 40], and allowing for the implementation of optimal control techniques developed for charge driven systems. Furthermore, we observe protection of the computational space from charge noise fluctuations affecting all other islands in the system, resulting from the reduction of the matrix elements for the two nearest transitions affecting the computational states ($|1\rangle \rightarrow |2\rangle$ and $|1\rangle \rightarrow |3\rangle$) for the rest of the circuit nodes $\{N_2, N_3\}$ (see Fig. 3(a)). The magnitude of flux matrix elements is also suppressed compared to implemented Fluxonium and Heavy Fluxonium devices ($|\langle \hat{\varphi} \rangle| \sim 1.5 - 2$) [27, 37], and due to the fact that flux fluctuations are typically around two orders of magnitude smaller than charge fluctuations in experimental setups [9], we will not expect them to represent a limiting factor.

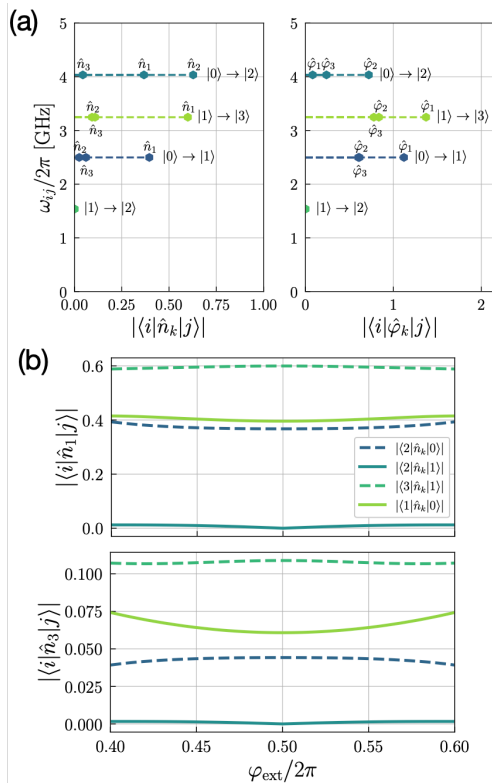


Figure 2: (a) Charge and flux-node operators matrix elements for all three islands in the system $\{N_1, N_2, N_3\}$ with respect to the transition frequencies, at the operation point $\varphi_{\text{ext}} = \pi$. (b) Change of \hat{n}_1 and \hat{n}_3 matrix elements, of interest for driving and measurement purposes, with respect to the external magnetic flux.

D. External Biases

In contrast to typical single-mode devices, the proposed system is susceptible to both external charge and flux bias. The susceptibility to external charge bias is due to the presence of a *charge-like* mode, or equivalently, a superconducting island coupled to the rest of the system only by capacitors and Josephson junctions, located in node N_2 of the circuit. The susceptibility to external flux is due to the presence of a closed loop formed by inductors and Josephson junctions, observed in the series connection of the branches $\{b_0, b_4, b_2\}$ (see Fig. 1(a)). The addition of the aforementioned effects can be modeled including

$$\begin{aligned} \hat{H}_{\text{ext}} = & 8 ([E_C]_{11}\hat{n}_2 + [E_C]_{01}\hat{n}_1 + [E_C]_{12}\hat{n}_3) n_{g_{\text{ext}}} \\ & + [E_L]_{b_2}\hat{\varphi}_3 \varphi_{\text{ext}} \end{aligned} \quad (2)$$

to the description, where $\{b_2\}$ was chosen as the closure branch of the inductive loop, $[E_C]_{ij}$ are the charging energies defined by the charge energy matrix and $[E_L]_{b_2} = \frac{1}{L_{b_2}} \left(\frac{\Phi_0}{2\pi}\right)^2$, with Φ_0 being the flux quantum. The effect of these external biases on the energy eigenvalues of the system is shown in Fig. 3.

Focusing on the effect of external flux bias, we observe a reduced dispersion around the operation point $\varphi_{\text{ext}} = \pi$. For fluctuations in external flux of around $10^{-2}\Phi_0$, we can observe a dispersion of less than 10 MHz. For comparison, in Fig. 3(c) we represent the energy dispersion from the operation

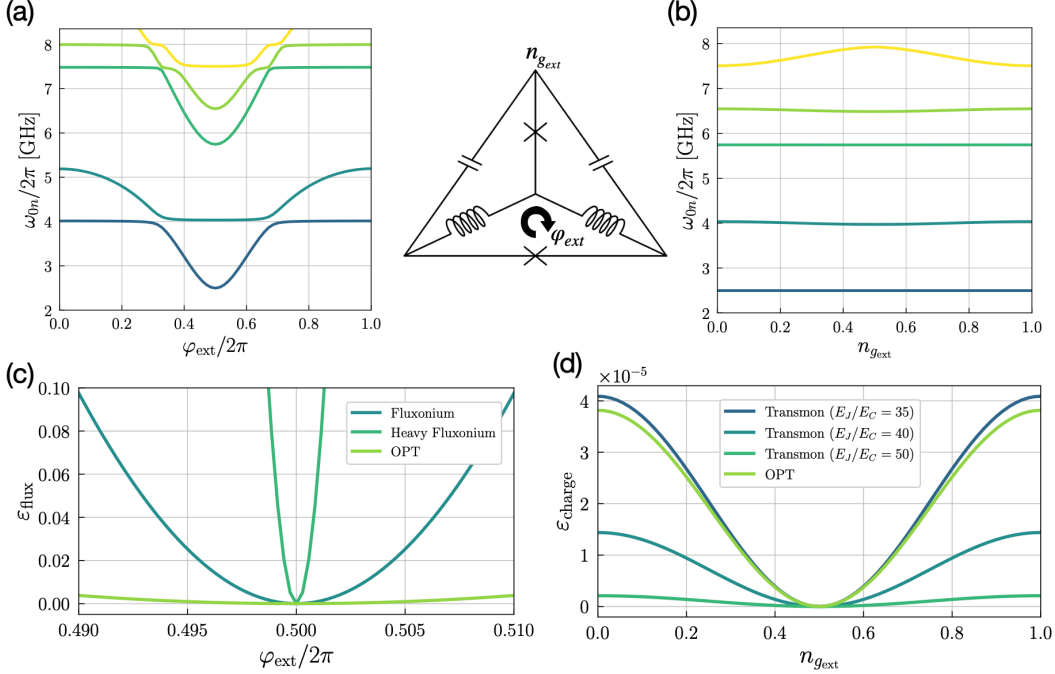


Figure 3: (a, b) Effect of external flux φ_{ext} and charge $n_{g_{ext}}$ bias, respectively, on the energy spectrum of the system. In ascending order, the energy difference $\omega_{0n} = \omega_n - \omega_0$ is shown for $n \in \{1, 2, 3, 4, 5\}$ for different values of external magnetic flux (charge) bias. (c, d) Energy dispersion with respect to external effects. (c) Plot of the energy dispersion $\varepsilon_{flux} = (\omega_{01} - \omega_{01}|_{\varphi_{ext}=\pi}) / (\omega_{01}|_{\varphi_{ext}=\pi})$ for different values of external flux bias around the operation point for the optimized device (OPT), in comparison with proposed Fluxonium [38] and Heavy Fluxonium [37] devices. (d) Plot of the energy dispersion $\varepsilon_{n_{g_{ext}}} = (\omega_{01} - \omega_{01}|_{n_{g_{ext}}=e}) / (\omega_{01}|_{n_{g_{ext}}=e})$ for different values of external charge bias, in comparison with different Transmon regimes.

point for several Fluxonium devices. We can observe that the proposed device expresses a dispersion of less than 0.5% from the qubit frequency, considerably small compared to other usually employed flux-sensitive devices [27, 37, 38].

When considering the effect of external charge bias, we observe that the dispersion is around 90 KHz, which is in the order of state-of-the-art charge-sensitive devices employed for quantum computation. In Fig. 3(d) we computed the energy dispersion due to external charge bias effect and checked that it accounts for a dispersion of 0.004% of the operation frequency. Furthermore, we compare with the Transmon device in different parameter regimes, showing dispersions in the order of the proposed device.

For completeness, we further present the dispersion of the charge operator matrix elements for nodes N_1 and N_3 in Fig. 2(b), showing a reduced fluctuation around the operation point $\varphi_{ext} = \pi$, suitable for gate operation and readout (see Sec. IV and V).

III. COHERENCE TIMES ESTIMATION

In order to perform an estimation of the coherence time of the device, focus has been made on the main decoherence channels considered in literature. In the estimation, different types of errors have been classified into two main categories, distinguishing between noises causing depolarization and dephasing.

A. Depolarization noise

To model the depolarization of the device due to different noise sources, we have employed the traditional expression derived from Fermi's Golden rule [20]. As the device on hand presents multiple elements, creating multiple branches \mathcal{B} , to compute the total coherence time we have computed the coherence times of every individual branch and added them together, to get a lower bound estimation [21, 22]. In general, for every depolarization chan-

nel, we will have

$$\Gamma_1^\lambda = \sum_{b_n \in \mathcal{B}} \sum_{ij} \frac{1}{\hbar^2} \left| \langle i | \hat{\mathcal{O}}_\lambda^{b_n} | j \rangle \right|^2 S_\lambda^{b_n}(\omega_{ij}), \quad (3)$$

where at least i or j correspond to one of the computational states $\{0, 1\}$, summing over all possible energy transitions into or out from the computational space, being $\hat{\mathcal{O}}_\lambda^{b_n}$ the operator coupling to the noise source and $S_\lambda^{b_n}(\omega_{ij})$ the power spectral density of the noise source. The consideration of all possible transitions involving at least one of the computational states, in contrast with other expressions used for single-mode devices, is due to the rich variety of possible transitions in the system, where depolarization due to excitation out of the computational space, although exponentially suppressed by the Boltzmann factor, can become one detrimental factor[21]. The main depolarization mechanisms considered are dielectric losses, inductive losses, and quasiparticle tunneling.

1. Dielectric losses

The appearance of an electric field across islands in the superconducting circuit causes the polarization of charges in the dielectric material to create electric dipole moments that cause dissipation [24]. To model this kind of loss we are going to consider the charge operator as coupling to the noise source $\hat{\mathcal{O}}_\lambda = -2e\hat{n}$ and a power spectral density of the form [23, 37]

$$S_{\text{Diel}}(\omega_{ij}) = \left(\frac{2\hbar}{CQ_{\text{Cap}}} \right) F(\omega_{ij}, T), \quad (4)$$

where

$$F(\omega_{ij}, T) = \frac{\coth\left(\frac{\hbar|\omega_{ij}|}{2K_b T}\right)}{1 + \exp\left(\frac{-\hbar\omega_{ij}}{K_b T}\right)}, \quad (5)$$

C represents the capacitor of the branch, Q_{Cap} is the quality factor of the capacitor, T is the assumed temperature of the device and K_b is the Boltzmann constant. The computed T_1^{Diel} times for different values of external flux are shown in Fig. 4(a). In the same figure, we display a comparison with Transmon device with a $E_J/E_C \sim 50$ relation and $E_C = 0.27$ GHz, which accounts for a capacitance of ~ 70 (fF), reasonably large considering usual qubit sizes of $\sim 600 - 800 \mu\text{m}^2$. We observe that the estimated depolarization time for the device at the operation point $\varphi_{\text{ext}} = \pi$ doubles the one expected for

the Transmon device assuming equal quality factors. Furthermore, we also compare with several Fluxonium devices, where the stronger suppression of the charge matrix elements produces an increase in coherence time, overcoming the T_1^{Diel} expressed by the proposed configuration at the cost of a decrease in manipulability.

2. Inductive losses

Similarly as for dielectric losses, we can consider the inductors of the system as having a lossy permeability inducing a frequency-dependent resistance [24]. To model this mechanism we considered the phase difference operator in every inductor $\hat{\mathcal{O}}_\lambda = \Phi_0 \hat{\varphi} / (2\pi)$ and a power spectral density of the form [23, 37]

$$S_{\text{Ind}}(\omega_{ij}) = \left(\frac{2\hbar}{LQ_{\text{Ind}}} \right) F(\omega_{ij}, T), \quad (6)$$

where L represents the inductance of the branch and Q_{Ind} accounts for the quality factor of the inductance. After computing the estimation for this loss mechanism we can appreciate that resistive loss in the inductors is not expected to represent the limiting decoherence mechanism in the device, obtaining coherence times on the order of milliseconds. This we believe is due to the lack of large valued inductances and consequently, small phase matrix elements, in contrast with other flux-sensitive devices where this noise mechanism is more notable.

3. Quasiparticle tunneling

The tunneling of quasiparticles in the Josephson junction elements is another well-known mechanism of dissipation and decoherence [26, 39]. To model this effect we consider the operator $\hat{\mathcal{O}}_\lambda = 2\Phi_0 \sin(\hat{\varphi}/2)$. To obtain a numerical representation of this operator in the charge basis, we performed a redefinition for the "charge-like" degree of freedom of N_2 , to the charge basis defined by single electrons instead of Cooper pairs [39] (see Appendix B). Additionally, a noise spectral density of the form

$$S_{\text{qp}}(\omega_{ij}) = 2\hbar\omega_{ij} \text{Re}\{Y_{\text{qp}}(\omega_{ij})\} F(\omega_{ij}, T), \quad (7)$$

was considered, where $\text{Re}\{Y_{\text{qp}}(\omega_{ij})\}$ can be approximated via the expression proposed in [15]. From numerical simulations, we appreciate that quasiparticle tunneling matrix elements vanish at the operation

point of $\varphi_{\text{ext}} = \pi$, similarly to previous flux sensitive devices proposed for operation at the sweet spot [15, 26]. Consequently, this depolarization mechanism is not expected to constitute one of the most detrimental factors constraining the coherence times.

B. Dephasing errors

For the estimation of the dephasing rate of the device, we are going to focus on one of the expected main contributions, which will come from the $1/f$ noise sources. These sources of noise are characterized by a power spectral density [27]

$$S_{1/f}^\lambda(\omega) = \frac{2\pi A_\lambda^2}{|\omega|}, \quad (8)$$

where, away from the sweet spot, they cause a dephasing rate of [4, 22, 27, 37]

$$\Gamma_{1/f}^\lambda = \sqrt{2}A_\lambda \left| \frac{\partial\omega_{01}}{\partial\lambda} \right| \sqrt{|\ln\omega_{\text{ir}}t|}. \quad (9)$$

1. $1/f$ flux noise

One of the main sources of decoherence in current flux-sensitive devices is the $1/f$ flux noise coming from the energy dispersion caused by the external magnetic flux φ_{ext} . For the estimation of the dephasing rate due to this noise source, we considered a reference value for the noise amplitude $A_{\varphi_{\text{ext}}}$ of $10^{-6}\Phi_0$, around the experimentally observed values [27, 41, 42], and we analytically computed the derivative of the qubit frequency from the Hamiltonian expression of Eq. 2 as $\partial\omega_{01}/\partial\Phi_{\text{ext}} = 1/\hbar \left[\langle 1|\partial\hat{H}_{\text{ext}}/\partial\Phi_{\text{ext}}|1\rangle - \langle 0|\partial\hat{H}_{\text{ext}}/\partial\Phi_{\text{ext}}|0\rangle \right]$ where $\partial\hat{H}_{\text{ext}}/\partial\Phi_{\text{ext}} = [E_L]_{b_2}(\hat{\varphi}_3 + \varphi_{\text{ext}}\mathbf{1})$. The estimated dephasing times for different values of external flux are shown in Fig. 4(b). We appreciate that the reduced energy dispersion causes an improvement in the estimated dephasing time. In the same figure, we compare with the estimated dephasing times for several Fluxonium devices, where this effect is one of the most detrimental for the total coherence time.

2. $1/f$ charge noise

Similarly, as for the flux mechanism, we considered the energy dispersion due to charge bias effects as a possible mechanism inducing dephasing. Due

to the reduced energy dispersion caused by external charge bias (see Fig. 3(d)), around 0.005% of the qubit frequency, this constitutes a minor decoherence channel, and after estimation, we observed that the coherence limit established by this mechanism is well above the one dictated from other decoherence channels.

C. T_2 times estimation

In order to add up all depolarization and dephasing effects, we consider the usual expression $T_2 = (1/2T_1 + 1/T_\varphi)^{-1}$, defining the total depolarization time as $T_1 = (1/T_1^{\text{Diel}} + 1/T_1^{\text{Res}} + 1/T_1^{\text{qp}})^{-1}$ and the total dephasing time as $T_\varphi = (1/T_\varphi^{\text{flux}} + 1/T_\varphi^{\text{charge}})^{-1}$. The estimated T_2 for different external flux values are shown in Fig. 4(c). We observe that around the operation point $\varphi_{\text{ext}} = \pi$, dielectric losses limit the coherence time. We appreciate improved robustness to magnetic flux fluctuations than Fluxonium devices away from the sweet spot, and larger coherence times than tunable Transmon up to fluctuations of $\sim 10^{-3}\Phi_0$. These coherence characteristics, considering the increase in anharmonicity and charge matrix elements, lead to a device with properties balancing noise resilience and controllability.

IV. SINGLE-QUBIT GATE

Having studied the selection rules and coherence properties of our multi-mode artificial atom, the next step is to analyze which are the gates to be implemented in the platform. In our case, in light of the selection rules of the circuit operators provided in Fig. 2(a), we aim to implement a $\{\mathcal{R}_x(\theta), \mathcal{R}_y(\theta)\}$ gate at shorter time t_g . We analyze the gate fidelity as well as the leakage channels. We assume charge-controlled quantum gates by driving a particular node. The Hamiltonian reads

$$\begin{aligned} \bar{\mathcal{H}} &= \sum_{k=0}^N \omega_k |k\rangle\langle k| + \Omega(t) \sum_{k>j} (\mathcal{O}_{k,j} |k\rangle\langle j| + \text{H.c.}) \quad (10) \\ \Omega(t) &= \Omega_X(t) \cos(\omega_d t) + \Omega_Y(t) \sin(\omega_d t) \quad (11) \end{aligned}$$

where ω_k is the energy of the k th energy level, $\mathcal{O}_{k,j} = n_{k,j} + im_{k,j}$ is the matrix element of the charge operator, and ω_d is the driving frequency. In light of the spectrum matrix in Fig. 1(b), we observe that the transition $|1\rangle \leftrightarrow |3\rangle$ is the nearest in frequency to the $|0\rangle \leftrightarrow |1\rangle$. Thus, following the typical quantum control procedure, where the system

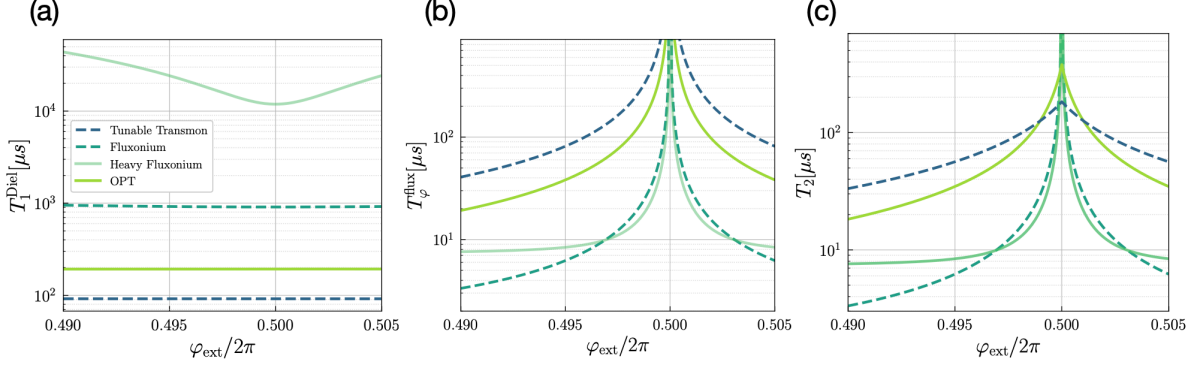


Figure 4: Coherence times estimation for the most detrimental decoherence channels. (a) T_1 estimation due to dielectric losses assuming $Q_{\text{Cap}} = 3 \cdot 10^6$ and $T = 15$ mK. (b) $T_{1/f}^{\text{Flux}}$ dephasing time estimation due to fluctuations of the external magnetic flux φ_{ext} , assuming $A_{\varphi_{\text{ext}}} = 10^{-6}\Phi_0$. (c) T_2 times estimation. For comparison, estimated coherence times for the optimized device (OPT), tunable Transmon $\{\omega_{01} \approx 5.2$ GHz, $E_J/E_C \approx 50$, $\gamma = 2.5\}$ [25], Fluxonium [38] and Heavy Fluxonium [37] devices are shown assuming equal quality factors and external fluctuation amplitudes.

is expressed in the rotating frame, will not capture the physics of our device. Instead, we express the Hamiltonian in the interaction picture with respect to $H = \sum \omega_k - \delta_k$, where the latter refers to the detuning between the driving and the transition to be addressed

$$\begin{aligned} \mathcal{H}(t) = & \sum_k \delta_k \\ & + \frac{[n_{0,1} + im_{0,1}][\Omega_X(t) - i\Omega_Y(t)]}{2} |0\rangle\langle 1| \\ & + \frac{[n_{1,3} + im_{1,3}][\Omega_X(t) - i\Omega_Y(t)]}{2} |1\rangle\langle 3| e^{i\alpha t} \\ & + \text{H.c.}, \end{aligned}$$

where $\alpha = \omega_3 - 2\omega_1$ is the energy of the main leakage channels. Here, we focus on the performance of X rotation so that the Hahn pulses are given by $\Omega_j(t) = \Omega_{0,j} \sin^2(\pi t/t_g)$. In this scenario, we choose the amplitude such that the Y on the $|0\rangle \leftrightarrow |1\rangle$ vanish, leading to

$$\begin{aligned} \mathcal{H}(t) = & \sum_k \delta_k + \frac{\lambda_1 \Omega_X(t)}{2} (|1\rangle\langle 0| + |0\rangle\langle 1|) \\ & + \frac{[\lambda_2 + i\lambda_3] \Omega_X(t)}{2} |1\rangle\langle 3| e^{i\alpha t} + \text{H.c.}, \end{aligned}$$

where $\lambda_1 = (n_{0,1}^2 + m_{0,1}^2)/n_{0,1}$, $\lambda_2 = \text{Re}\{(m_{0,1} + in_{0,1})(m_{1,3} - in_{1,3})\}$ and $\lambda_3 = \text{Im}\{(m_{0,1} + in_{0,1})(m_{1,3} - in_{1,3})\}$ stand for the dressed matrix elements of the control Hamiltonian. Fig. 5(a) shows the gate error $\mathcal{E}(U, V) = 1 - \mathcal{F}(U, V)$ for implementing an X rotation using the typical

Hahn pulse for different gating time $t_g \in \{5, 20\}$ [ns], where \mathcal{F} is the gate fidelity defined as [43]

$$\mathcal{F}(U, V) = \frac{\text{Tr}[U_q U_q^\dagger]}{d(d+1)} + \frac{|\text{Tr}[U_q V^\dagger]|^2}{d(d+1)} \quad (12)$$

Here, U_q represents the truncated unitary operator in the computational subspace, and $V \equiv \{X, Y\}$ is the gate to be implemented. From the figure, we observe smaller gate errors around $\mathcal{E} = 3.02 \times 10^{-4}$ for the shorter gate time $t_g = 5$ ns and $\mathcal{E} = 5.72 \times 10^{-7}$ for the longer $t_g = 20$ ns. We attribute such small gate errors at shorter gate time to the absence of the typical leakage channel $|1\rangle \leftrightarrow |2\rangle$, which is zero for the charge operator \hat{n}_1 in accordance with Fig. 2. We should note that the important leakage channel in our architecture corresponds to the $|1\rangle \leftrightarrow |3\rangle$ transition which we cannot neglect with the RWA since its matrix elements and detuning from the computational subspace (~ 750 MHz) does not hold the RWA criteria for short gate times. To quantify the error produced by this outlier transition, we compute the leakage error from the k -th computational state, defined as

$$\mathcal{L}_{|k\rangle} = \frac{1}{d} \sum_{k \neq j=2}^N \left[|\langle j|U|k\rangle|^2 + |\langle k|U|j\rangle|^2 \right]. \quad (13)$$

Fig. 5(b) shows the leakage for the first excited state $\mathcal{L}_{|1\rangle}$ for the X gate as a function of the gating time t_g . Similar to the gate error, we observe reduced amount of leakage even for shorter gating time. For our gating time range, we observe maximal and minimal

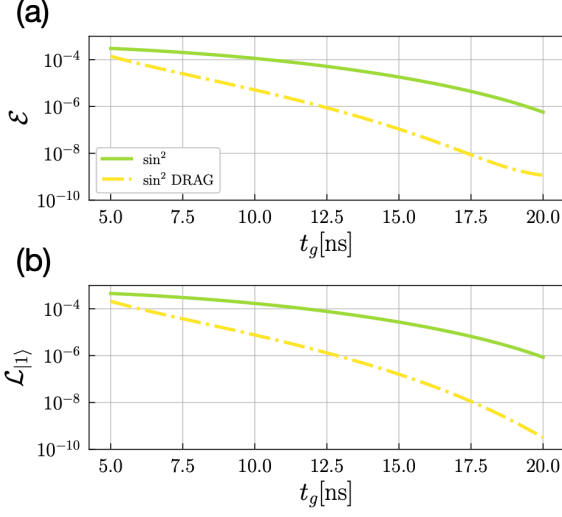


Figure 5: (a) Total gate fidelity and (b) leakage rates versus gating time. Green solid lines represent the gate error and leakage using standard Hahn pulse, while dashed dotted yellow lines represent the same dynamics but by using the DRAG correction.

leakage equal to $\mathcal{L}_{|1\rangle} = \{4.54 \times 10^{-4}, 8.56 \times 10^{-7}\}$, respectively. A way to reduced leakage relies on using pulse shaping techniques as the Derivative Removal by Adiabatic Gates (DRAG) [44]. In this framework, we aim for eliminating leakage contributions through perturbative diagonalization provided by the generator

$$\hat{S}(t) = \frac{\epsilon \Omega(t)}{2\alpha} \left[\beta \lambda_1 |0\rangle\langle 1| + (\lambda_2 + i\lambda_3) |1\rangle\langle 3| e^{i\alpha t} \right] - \text{H.c.}, \quad (14)$$

where $\epsilon = 1/(t_g \alpha)$ is the perturbation parameter useful for order counting in the effective Hamiltonian, $\Omega(t)$ is the corrected pulse amplitude, and β is a free parameter that controls which type of error DRAG can correct [45]. With this generator, the effective second-order Hamiltonian reads

$$\mathcal{H}_{\text{eff}}(t) = \mathcal{H}(t) + [\hat{S}(t), \mathcal{H}(t)] + \frac{1}{2} [[\hat{S}(t), \mathcal{H}(t)], \mathcal{H}(t)] + i\dot{\hat{S}}(t), \quad (15)$$

which at second order in ϵ has the following structure

$$\mathcal{H}_{\text{eff}}(t) = \begin{bmatrix} -\frac{\epsilon^2 \beta \lambda_1^2 \Omega \text{Re}\{\Omega_X\}}{2\alpha} & \frac{\epsilon \lambda_1}{2} \left[\Omega_X - i \frac{\beta \dot{\Omega}}{\alpha} \right] & 0 & \frac{\epsilon^2 (1-\beta) \lambda_1 (\lambda_2 + i\lambda_3) \Omega \Omega_X e^{-i\alpha t}}{4\alpha} \\ \frac{\epsilon \lambda_1}{2} \left[\Omega_X^* + i \frac{\beta \dot{\Omega}^*}{\alpha} \right] & \delta_1 + \frac{\epsilon^2 (\beta \lambda_1^2 - \lambda_2^2 - \lambda_3^2) \Omega \text{Re}\{\Omega_X\}}{4\alpha} & 0 & \frac{\epsilon (\lambda_2 + i\lambda_3)}{2} \left[\Omega_X - \Omega - i \frac{\dot{\Omega}}{\alpha} \right] e^{-i\alpha t} \\ 0 & 0 & \delta_2 & 0 \\ \frac{\epsilon^2 (1-\beta) \lambda_1 (\lambda_2 - i\lambda_3) \Omega^* \Omega_X^* e^{i\alpha t}}{4\alpha} & \frac{\epsilon (\lambda_2 - i\lambda_3)}{2} \left[\Omega_X^* - \Omega^* + i \frac{\dot{\Omega}^*}{\alpha} \right] e^{i\alpha t} & 0 & \delta_3 + \frac{\epsilon^2 (\lambda_2^2 + \lambda_3^2) \Omega \text{Re}\{\Omega_X\}}{4\alpha} \end{bmatrix} \quad (16)$$

where $*$ refers to complex conjugate. From the effective Hamiltonian, we can eliminate leakage to the $|1\rangle \leftrightarrow |3\rangle$ transition by choosing the control to be

$$\Omega_X(t) = \Omega(t) + i \frac{\dot{\Omega}(t)}{\alpha}. \quad (17)$$

We should note that independently of the value of the parameter β , the DRAG correction eliminates up to second order in ϵ for the $|1\rangle \leftrightarrow |3\rangle$ leakage channel. Then, the beta parameter can be set such that we minimize the phase error on the gate. To do so, consider the difference between the diagonal elements of the effective Hamiltonian in the qubit subspace

$$\mathcal{H}_{\text{eff}}[1, 1] - \mathcal{H}_{\text{eff}}[0, 0] = \delta_1 + \frac{\epsilon^2 (2\beta \lambda_1^2 - \lambda_2^2 - \lambda_3^2) |\Omega|^2}{4\alpha}, \quad (18)$$

We can eliminate the phase accumulation by setting $\delta_k = k(\delta \epsilon^2)$, obtaining

$$\delta = -\frac{|\Omega(t)|^2 (2\beta \lambda_1^2 - \lambda_2^2 - \lambda_3^2)}{2\alpha}. \quad (19)$$

The validity of δ_k relies on the effective Hamiltonian, where diagonal terms come from even commutators which scale as ϵ^{2j} . Thus, a time-dependent detuning is able to eliminate (also at second order in ϵ) the phase error on our gate. Another alternative without relying on time-dependent detuning consist in setting β such that the phase from the qubit subspace destructively interfere. For our control, the optimal value is given by

$$\beta = \frac{\lambda_2^2 + \lambda_3^2}{2\lambda_1^2}. \quad (20)$$

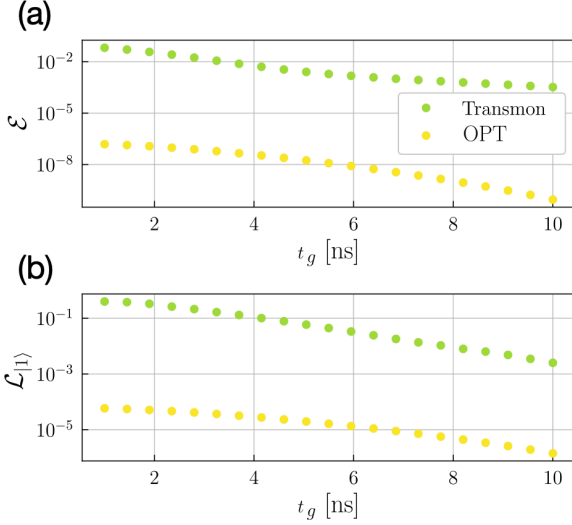


Figure 6: Gate error \mathcal{E} and leakage $\mathcal{L}_{|1\rangle}$ as a function of the gating time t_g by optimizing the pulse parameters $\{\Omega_0, \delta\}$. For comparison, results for the optimized device (OPT) and Transmon device are shown.

For Transmon circuit we have that the control Hamiltonian satisfies $\lambda_1 = 1$, $\lambda_2 = \sqrt{2}$, and $\lambda_3 = 0$ so that the optimal β reducing the phase error is $\beta = 1/2$, such variation of the DRAG pulse is known as half-DRAG [45]. Notice that either using time-dependent detuning or setting the β in the optimal configuration, we should be able to reduce phase error. However, from the effective Hamiltonian, choose $\beta \neq 1$ induces leakage between the $|0\rangle \leftrightarrow |3\rangle$ transition, which for shorter gating time should also reduce the performance of the gate.

Fig. 5(a) and Fig. 5(b) show the gate error $\mathcal{E}(X, U)$ and the leakage to the first excited state $\mathcal{L}_{|1\rangle}$ as a function of the gating t_g using the DRAG correction with $\beta = 1$. From the figure, we appreciate remarkable suppression of both leakage and gate error for gating time longer than 5 ns, for the shorter gating time we obtain a 2-fold improvement in both quantities while at 20 ns the enhancement is more than three orders of magnitude. Thus, our architecture should be able to implement single-qubit gates close-to-unit fidelity in gating times below 15 ns.

For achieving smaller gate error in single-qubit gates below the $t_g = 10$ ns, we can use typical control strategies such as: considering a non-resonant drive $\omega_d = \omega_{10} + \delta_1$ and find the optimal detuning that cancel out most of the phase error [47]. Additionally, we can optimize over the drive amplitude Ω_0 and choosing the DRAG parameter β to be the one fulfilling Eq. (20). The numerical optimization

were performed using the Nelder-Mead subroutine included in the `scipy.minimize` package [28]. We compare our findings with the same gate performed on Transmon circuits with typical parameters $\omega_{10} = 2\pi \times 5$ GHz, and $\alpha = -2\pi \times 250$ MHz [4].

Fig. 6 shows the gate error \mathcal{E} and the leakage $\mathcal{L}_{|1\rangle}$ as a function of the gating time resulting from the optimization process for both devices. From the figure, we observe that our architecture performs better than the Transmon thanks to the cancellation of $|1\rangle \leftrightarrow |2\rangle$ leakage channel; and due to having an anharmonicity with the closest transition of 750 MHz, three times larger than the anharmonicity expressed by the Transmon. Our optimized dynamics shows gate error around $\mathcal{E} = 10^{-8}$ for an X gate at $t_g = 5$ ns. Furthermore, we also observe leakage reduction, but it is smaller than the increase of the gate fidelity, therefore, it is possible to conclude that for shorter gating time $t_g = (5, 10)$ ns, phase accumulation is the dominant source of error.

V. READOUT AND ACTIVE RESET

The next step in the characterization of our multi-mode qubit corresponds to study the dispersive readout when it is coupled to a transmission line resonator [29]. Due to the multi-level nature of the artificial atom in cQED architecture, we denote as $|k\rangle$ and ϵ_k as the k th states and energies of the circuit, respectively. In this basis, the Hamiltonian reads

$$\begin{aligned} \mathcal{H} = & \sum_k \epsilon_k |k\rangle\langle k| + \omega_r \hat{a}^\dagger \hat{a} + \Omega(t) \cos(\omega_r t) (\hat{a}^\dagger + \hat{a}) \\ & + \sum_{k,k'} g_{k,k'} |k\rangle\langle k'| (\hat{a}^\dagger + \hat{a}), \end{aligned} \quad (21)$$

here, $g_{k,k'} = g \langle k | \hat{n}_3 | k' \rangle / |\langle 0 | \hat{n} | 1 \rangle|$ is the dressed charge coupling strength for the node $\{3\}$ and $\Omega(t)$ the envelope of the microwave drive used for the readout. We can simplify the Hamiltonian by expressing it in the rotating frame with respect to the drive frequency, and eliminate the counter-rotating terms through the rotating wave approximation, leading to the generalized Jaynes-Cummings model

$$\begin{aligned} \mathcal{H}_{\text{JCM}} = & \sum_k (\epsilon_k - \omega_r k) |k\rangle\langle k| + \frac{\Omega(t)}{2} (\hat{a}^\dagger + \hat{a}) \\ & + \sum_k g_k (|k\rangle\langle k+1| \hat{a}^\dagger + |k+1\rangle\langle k| \hat{a}). \end{aligned} \quad (22)$$

For typical resonator frequencies $\omega_r = 2\pi \times 6.990$ GHz [48], we obtain cavity-qubit detuning

$\Delta_{10} = |\omega_1 - \omega_0 - \omega_r| = 2\pi \times 4.502$ GHz which for coupling strength $g_1 = 2\pi \times 37$ MHz allows us to operate in the dispersive regime, where the Hamiltonian is diagonal up to second order in the expansion parameter $\bar{\chi}_1 = g^2/\Delta_{10}$

$$\mathcal{H}_{\text{eff}} = \sum_k (\epsilon_k - \omega_r k) |k\rangle\langle k| + \sum_k \chi_k |k\rangle\langle k| \hat{a}^\dagger \hat{a} + \frac{\Omega(t)}{2} (\hat{a}^\dagger + \hat{a}). \quad (23)$$

Here, $\chi_k = \sum_\ell [\bar{\chi}_{k,\ell} - \bar{\chi}_{\ell,k}]$ is the total dispersive shift taking into account the multi-level nature of our device, with $\bar{\chi}_{\ell,k} = |g_{\ell,k}|^2/(\epsilon_{\ell,k} - \omega_r)$ being the state-dependent Stark-shift. Notice that for artificial atoms truncated in the qubit subspace, we obtain the typical Stark-shift of the form $\chi_1 = \bar{\chi}_1$. Nevertheless, by including outlier energy levels, the Stark-shifts modifies as $\chi_1 = g_1^2/\Delta_{10} - g_2^2/(2\Delta_{21})$ [30], obtaining a smaller contrast between the computational states. Thus, we need to choose the adequate charge node for implementing the readout. Thanks to the multi-mode nature of the device we can choose different nodes for different operations. In particular in our device, we set the node $\{1\}$ for driving purposes while the remaining could be used for readout by coupling either an additional resonator or Purcell filters [31]. Thus, we have to decide if we use node $\{2\}$ or node $\{3\}$. In light of Fig. 2 we see that the matrix elements of the node $\{3\}$ have larger values than the second one, so that the capacitive coupling is stronger allowing to achieve better contrast χ and consequently faster readout. To understand how the measurement works, let us consider the Heisenberg equation of motion for the cavity operator \hat{a} . In this derivation, we do not consider qubit decay or dephasing. In this scenario, the equation of motion reads

$$\dot{\langle \hat{a} \rangle} = i\chi_k \langle \hat{a} \rangle - \frac{\kappa}{2} \langle \hat{a} \rangle + i\Omega(t), \quad (24)$$

where κ is the decay rate of the resonator. For a constant drive, $\Omega(t) = \Omega$, and the resonator initialized in the vacuum, we obtain and steady state solution of the form

$$\langle \hat{a}(t) \rangle = -\frac{4\chi_k \Omega}{\kappa^2 + 4\chi_k^2} + i\frac{2\kappa \Omega}{\kappa^2 + 4\chi_k^2} \quad (25)$$

That represents the position of the multi-level system in the IQ plane of the resonator. Thus, different states may arrive to different points of such plane, which could be maximized depending on the microwave envelope to be used. In our case, we consider a pulse of the form $\Omega(t) = \Omega_0 \sin^3(\pi t/t_m)$, where Ω_0

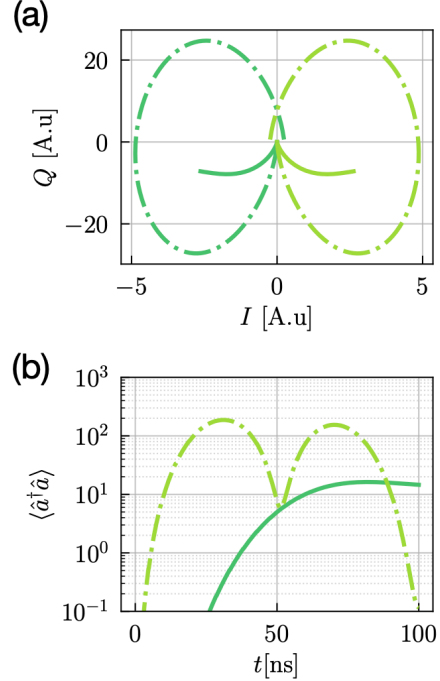


Figure 7: (a) Evolution of the IQ plane of the resonator dispersively coupled to our multi-mode architecture under two different pulse sequences: Gaussian pulse (green solid lines) and the corrected with the DRAG mechanism (dashed dotted lines). (b) Photon number stored on the resonator as a function of the measurement time for the Gaussian and the DRAG corrected pulses. The simulation parameters are given by $\omega_r = 2\pi \times 6.99$ GHz, $\epsilon_{10} = 2\pi \times 2.5$ GHz, $g = 2\pi \times 87$ MHz.

is the pulse strength and $t_m = 100$ ns is the measurement time. We calibrate $\Omega_0 = 2\pi \times 35.39$ MHz such that the number of photon stored in the resonator be equal to five at the middle of the dynamics. We will characterize the readout process in terms of two factors: (a) contrast between the qubits state on the IQ plane at the middle of the readout, (b) smaller left-over qubit population and photon number at the end of the readout. We expect an empty cavity for reuse, and qubit population similar than at the beginning of the protocol.

Fig. 7(a) show the trajectory on the IQ plane for the computational states of our device in the multi-level approximation. The figure shows that the displacement of the state along the phase space of the resonator is mainly along the Q axis which agrees with the steady state solution since the decay rate of the resonator is larger than the Stark-shift in the dispersive model i.e., $\kappa = 9.03\chi_1$. Moreover, Fig. 7(b) also shows the photon number stored on the res-

onator for the system being initialized in $|e\rangle$. From the figure, we appreciate that: (a) The resonator is driven in such a way that its critical photon number $\bar{n}_{\text{crit}} \equiv [\Delta_{10}/(2g_1)]^2 \equiv 11\text{K}$ is not exceeded, and the multi-mode system be not driven outside the potential for avoiding ionization phenomena [32], so that non-linearities as Kerr effect does not play a role in the measurement outcome [33], and (b) the enveloped $\Omega(t) = \Omega_0 \sin^3(\pi t/t_m)$ even though it vanishes at $t = t_m$, the leftover photon number does not decrease during the evolution. Thus, for an active use the of the multi-mode qubit we need to implement an active/passive reset mechanism.

The reset mechanism to be analyzed is the same as in Ref. [34], which relies on using DRAG-like pulses to reversed engineering the resonator's transfer function, guaranteeing at the same time reduced leftover photon and qubit population. The starting point is the input-output equation of motion for the resonator operator, expressed in the Fourier domain

$$i\omega\bar{a}(\omega) = i\chi_k\bar{a}(\omega) - \frac{\kappa}{2}\bar{a}(\omega) + i\bar{\Omega}(\omega) - \sqrt{\kappa}\bar{a}_{\text{in}}(\omega),$$

where the bar variables are the Fourier transformed function, and $\bar{a}_{\text{in}}(\omega)$ is the input field on the transmission line resonator. We have many input-output relation as states in our multi-mode qubit. In our derivation, we will fix a single value of χ_k , and the generalization to higher states is straightforward. On the other hand, in absence of the drive, we write the input field as

$$\bar{a}_{\text{in}}(\omega) = \frac{1}{\sqrt{\kappa}} \left[i(\omega - \chi_k) + \frac{\kappa}{2} \right] \bar{a}(\omega), \quad (26)$$

That corresponds to the inverse of the transfer-function of the qubit-resonator transfer function $T(\omega)_{|k}^{-1}$. If we choose the drive envelope to be

$$\bar{\Omega}(\omega) = -\frac{i}{\sqrt{\kappa}} \left[i(\omega - \chi_k) + \frac{\kappa}{2} \right] \bar{\Omega}_{\text{trial}}(\omega), \quad (27)$$

where $\bar{\Omega}_{\text{trial}}(t) = \Omega_0 \sin^3(\pi t/t_m)$ is a trial function to be optimized. This selection allows us to obtain zero output field $\bar{a}(\omega) = 0$ at the end of the measurement time when the system is initialized in the state $|k\rangle$. For correcting several qubit states, the pulse envelope reads

$$\bar{\Omega}(\omega) = \prod_{k=0}^N T(\omega)_{|k}^{-1} \bar{\Omega}_{\text{trial}}(\omega), \quad (28)$$

Fig. 7(a) shows the state displacement on the IQ plane using our corrected pulse, showing that during

the readout the states are far away from each other increasing the contrast and the distinguishability of the qubit states. Moreover, the corrected pulse also allows the states to come back to the origin of the IQ plane representing the active reset mechanism. Likewise, Fig. 7(b) and (c) compares the photon number and the probability of the qubit state under the corrected/uncorrected pulse. For both cases (leftover photon and qubit population), we see a reduction of two order of magnitudes of these values at the end of the readout process.

VI. RESILIENCE TO PARAMETER FLUCTUATIONS

The proposed device relies on a certain parameter regime in order to express the desirable characteristics studied in the previous chapters. For that reason, in this section we focus on studying how fluctuations in physical values of the components constituting the circuit, expected from fabrication inaccuracies, modify the characteristics of the device. For that purpose we computed the system characteristics, for multiple circuit instances modifying the capacitances, Josephson junction energies, and linear inductances, considering normal distributions around the optimal values for different degrees of standard deviation. In Fig. 8 we show the variation of the anharmonicity, charge and flux dispersion under different degrees of deviation, compared to Transmon and Fluxonium devices. We observe that under reasonable values of deviation expected from fabrication, the desired characteristics of the device are preserved, thus accounting for certain fabrication resilience of the obtained solution. As a proof of concept on fabrication, in Appendix C we present a lithographic proposal of the device, optimized to fulfill the capacitive relations obtained in the theoretical design optimization, where the capacitive relations are matched with an estimated error smaller than $\sim 10\%$. This capacitive mismatch could also be decreased by considering the extra capacitance induced by the introduction of the junction and junction arrays to the design, so that a lower-shooting approach to match the capacitive relations could be beneficial.

VII. TOWARDS SCALABILITY

A crucial aspect to consider when engineering superconducting qubits is scalability. Proposals for novel superconducting qubits have primarily focused

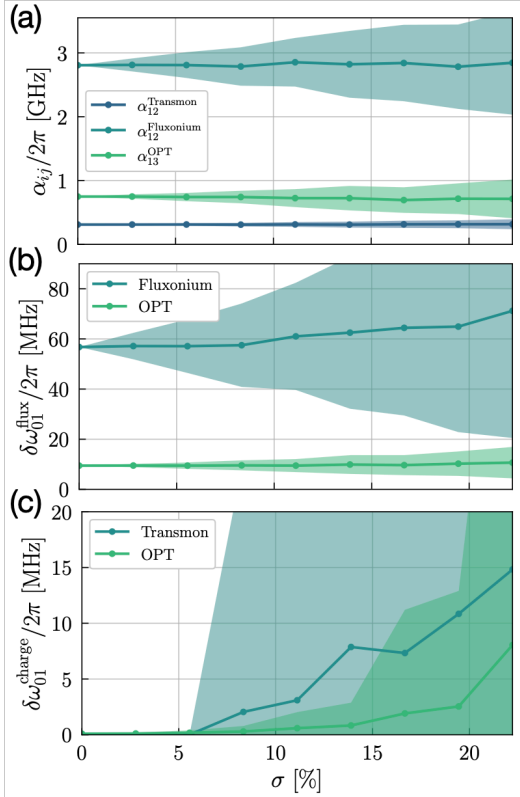


Figure 8: Resilience to parameter fluctuations simulation. Mean values and standard deviation of (a) anharmonicity α_{ij} , (b) energy dispersion for $10^{-2}\Phi_0$ flux fluctuations $\delta\omega_{01}^{\text{flux}}$, and (c) energy dispersion for e^- charge fluctuations $\delta\omega_{01}^{\text{charge}}$, for 500 circuits instances with values taken from a normal distribution around the optimal physical values considering different standard deviation σ of the normal distributions.

on improving the coherence time of the computational space by reducing the charge (flux) matrix elements involving the computational states. This approach reduces the coupling of the system to both the environment and other circuit components. Although this method effectively improves coherence, it has the side effect of significantly reducing manipulability. This reduction causes problems in the implementation of single-qubit gates, as it imposes the necessity of either a strong capacitive coupling to the circuit or powerful external drives. Therefore, it is important to balance the coupling elements so that the device remains protected yet addressable.

This effect is even more significant when considering two-qubit operations, as the coupling between the qubits decreases quadratically with the reduction in matrix elements. This is a crucial limiting

factor in scaling protected devices such as (Heavy) Fluxonium, Zero-pi, Bifluxon, etc. Conversely, for the Transmon, the large matrix elements facilitate its coupling to other qubits; however, its relatively limited T_1 times constrain the total coherence times. The balance found for the matrix elements of the qubit proposed here takes a step forward toward finding proper configurations suitable for the implementation of two-qubit operations, while maintaining sufficiently relevant anharmonicity and coherence times, thereby decreasing the ratio between the gate time and the total coherence time.

VIII. SUMMARY AND CONCLUSION

In this article, we presented a superconducting device based on a multi-mode structure, the Difluxmon qubit. We studied the main characteristics of the system, which were optimized to fulfill the requirements for performing quantum computation. The proposed device was designed to overcome the limiting factors that constrain the coherence time of the most widely used superconducting qubit devices: Transmon and Fluxonium.

The two main factors limiting the coherence times and coherent operation of the Transmon qubit are dielectric losses and leakage out of the computational space. By engineering the matrix elements of charge and flux operators, we were able to increase the T_1 while maintaining sufficiently high values to perform fast quantum operations without requiring large coupling to the system or strong drives. Furthermore, an enhancement in anharmonicity was achieved, allowing for faster and more coherent gate operations by decreasing leakage. The main factors limiting Fluxonium coherence and manipulability are the large dephasing rate, the suppression of the charge matrix elements, and the low qubit frequency. The proposed configuration presents a reduced energy dispersion at the operation point $\varphi_{\text{ext}} = \pi$, resulting in enhanced dephasing time. Additionally, the charge matrix elements exhibit increased values, sacrificing T_1 coherence compared to Fluxonium systems, but improving manipulability. This improvement could be significant for superconducting quantum processors, as the increase of approximately a factor of 3 over usual Fluxonium charge matrix element values could be crucial for coupling multiple qubits together.

In contrast to topologically protected qubits, the proposed device does not rely on creating a fully protected subspace to encode quantum information but rather on reducing decoherence in the computational space while maintaining manipulability. This ap-

proach allows for simpler driving methods and avoids more complex procedures that could alter the system's coherence properties.

Regarding controllability, we performed gate simulations for different pulse durations and analyzed the performance of DRAG techniques extended for multi-level systems. When characterizing the speed limit in gate operation, we must consider two important limiting factors: the limit set by the system anharmonicity α and the limit established by the qubit frequency ω_q . The proposed device presents an anharmonicity of $|\alpha|/2\pi \approx 750$ MHz, which sets a fundamental gate speed limit of approximately 1.4 ns. The qubit frequency ω_q establishes another limit, as we require the system's Larmor period to be much larger than the gate time ($t_g \times \omega_q$) $\gg 1$. The fundamental limit in gate time for the proposed device balances both requirements. This, combined with the use of optimal control techniques (DRAG), allows for fast coherent operations, setting the manipulation speed limit within the instrumental capabilities. Additionally, we have presented an active reset scheme and showed that by properly choosing the coupling point to the circuit, we can increase the I-Q plane separation and thereby improve the readout fidelity.

Resilience to fabrication errors is another limiting aspect in many multimode device proposals. In this work we have studied how fluctuations in the device parameters alter the system characteristics, showing at least equal resilience than single mode devices under reasonable fabrication deviations.

The ability to engineer characteristics such as the enhancement of the anharmonicity and the coherence times while simultaneously keeping matrix elements sufficiently large can be crucial for scaling up towards multi-qubit quantum processors. Devices with larger T_1 protection may find limitations when coupled together, due to the difficulty of achieving strong coupling and performing sufficiently fast two-qubit operations. The Difluxmon finds a combination of characteristics from Transmon, i.e. sufficiently large charge matrix elements; and Fluxonium, i.e. larger anharmonicity and longer T_1 times; which can be an important step towards finding proper tradeoffs suitable to construct larger processing units. Remarkably, with this device we have shown that by relying in a multi-mode structure, the need for heavy (light) charge (flux) modes in order to achieve longer coherence times relaxes and coherent devices with reasonable component values, can be found, striking a balance between manipulability, fabrication requirements, and noise protection.

ACKNOWLEDGEMENTS

The authors would like to thank Frederik Pfeiffer and Christian Schneider for useful discussions and insightful comments. The authors acknowledge support from and HORIZONCL4-2022-QUANTUM01-SGA project 101113946 OpenSuperQPlus100 of the EU Flagship on Quantum Technologies. F. A. C. L acknowledges support from the German Ministry for Education and Research, under QSolid, Grant no. 13N16149. M. S. acknowledges support from the Spanish Ramon y Cajal Grant RYC-2020-030503-I, project Grant No. PID2021-125823NA-I00 funded by MCIN/AEI/10.13039/501100011033 and by "ERDF A way of making Europe" and "ERDF Invest in your Future", and from the IKUR Strategy under the collaboration agreement between Ikerbasque Foundation and BCAM on behalf of the Department of Education of the Basque Government. This project has also received support from the Spanish Ministry of Economic Affairs and Digital Transformation through the QUANTUM ENIA project call - Quantum Spain, and by the EU through the Recovery, Transformation and Resilience Plan - NextGenerationEU and Basque Government through Grant No. IT1470-22, through the ELKARTEK program, project KUBIT (KK-2024/00105). P. G. A. acknowledges support from UPV/EHU Ph.D. Grant No. PIFG 22/25. G. R. acknowledges Dicyt USACH under grant 5392304RH-ACDicyt and Financiamiento Basal para Centros Científicos y Tecnológicos de Excelencia (Grant No. AFB220001).

Appendix A: Hamiltonian Derivation

The Lagrangian description of the circuit presented in Fig. 1(a), considering node $\{0\}$ as reference, is given by

$$\begin{aligned} \hat{\mathcal{L}} = & \frac{1}{2} \dot{\boldsymbol{\phi}}^T \mathbf{C} \dot{\boldsymbol{\phi}} - \frac{1}{2} \boldsymbol{\phi}^T \mathbf{L}^{-1} \boldsymbol{\phi} + E_J^{b_0} \cos\left(\frac{2\pi}{\Phi_0} \hat{\phi}_1\right) \\ & + E_J^{b_5} \cos\left(\frac{2\pi}{\Phi_0} (\hat{\phi}_2 - \hat{\phi}_3)\right), \end{aligned} \quad (\text{A1})$$

where $\boldsymbol{\phi}^T = (\hat{\phi}_1, \hat{\phi}_2, \hat{\phi}_3)$ is the flux-node vector. The capacitance and inductance matrices are given by

$$\mathbf{C} = \begin{pmatrix} C^{b_0} + C^{b_3} + C^{b_4} & -C^{b_3} & -C^{b_4} \\ -C^{b_3} & C^{b_1} + C^{b_3} + C^{b_5} & -C^{b_5} \\ -C^{b_4} & -C^{b_5} & C^{b_2} + C^{b_4} + C^{b_5} \end{pmatrix}, \quad (\text{A2})$$

$$\mathbf{L}^{-1} = \begin{pmatrix} 1/L_{b^4} & 0 & -1/L_{b^4} \\ 0 & 0 & 0 \\ -1/L_{b^4} & 0 & 1/L_{b^2} + 1/L_{b^4} \end{pmatrix}. \quad (\text{A3})$$

Performing a Legendre transform we can obtain the Hamiltonian of the system, given by

$$\begin{aligned} \hat{H} = & \frac{1}{2} \mathbf{q}^T \mathbf{C}^{-1} \mathbf{q} + \frac{1}{2} \boldsymbol{\phi}^T \mathbf{L}^{-1} \boldsymbol{\phi} - E_J^{b_0} \cos\left(\frac{2\pi}{\Phi_0} \hat{\phi}_1\right) \\ & - E_J^{b_5} \cos\left(\frac{2\pi}{\Phi_0} (\hat{\phi}_2 - \hat{\phi}_3)\right). \end{aligned} \quad (\text{A4})$$

By performing the change to dimensionless variables $\hat{q} = 2e \hat{n}$ and $\hat{\phi} = \frac{\Phi_0}{2\pi} \hat{\phi}$, we can rewrite

$$\begin{aligned} \hat{H} = & 4 \mathbf{n}^T \mathbf{E}_C \mathbf{n} + \frac{1}{2} \boldsymbol{\varphi}^T \mathbf{E}_L \boldsymbol{\varphi} - E_J^{b_0} \cos(\hat{\varphi}_1) \\ & - E_J^{b_5} \cos(\hat{\varphi}_2 - \hat{\varphi}_3), \end{aligned} \quad (\text{A5})$$

with $[E_C]_{ij} = \frac{e^2}{2}[C^{-1}]_{ij}$ and $[E_L]_{ij} = \left(\frac{\Phi_0}{2\pi}\right)^2 [L^{-1}]_{ij}$. In order to complete the description, we should include the effect of external biases on the system. In every island of the system N_i with $i \in \{1, 2, 3\}$ we may experiment an external charge bias $[n_{g_{ext}}]_i$. Considering this bias to be static in time, we can always make a proper choice of gauge to eliminate it in "flux-like" degrees of freedom [36], keeping only the contribution to the "charge-like" degree of freedom of our system N_2 , so that we can represent its effect by making the substitution $\hat{n}_2 \rightarrow \hat{n}_2 + n_{g_{ext}}$ in the Hamiltonian description in Eq. A5. For the introduction of the external flux effect to the model, we should consider every inductive loop in the system. The single inductive loop in the device is the one produced by the series connection of the branches $\{b_0, b_4, b_2\}$. To reflect the effect of external magnetic flux bias threading the loop we include an extra static constant φ_{ext} in the linear inductor term of the branch b_2 , selected as the one closing the loop. All the described effects can be modeled, including the term

$$\begin{aligned} \hat{H}_{\text{ext}} = & 8 ([E_C]_{11} \hat{n}_2 + [E_C]_{01} \hat{n}_1 + [E_C]_{12} \hat{n}_3) n_{g_{\text{ext}}} \\ & + [E_L]_{b_2} \hat{\varphi}_3 \varphi_{\text{ext}}, \end{aligned} \quad (\text{A6})$$

to the Hamiltonian description in Eq. A5.

Appendix B: Numerical simulation

To implement the Hamiltonian numerically, we distinguish between *charge-like* and *flux-like* modes.

The former ones are represented in the so-called charge basis where operators are represented as

$$\begin{aligned} \hat{n} &= \sum_{n=-N_c}^{N_c} n |n\rangle \langle n|, \\ \cos(\hat{\varphi}) &= \sum_{n=-N_c}^{N_c} \frac{1}{2} (|n+1\rangle \langle n| + |n\rangle \langle n+1|), \\ \sin(\hat{\varphi}) &= \sum_{n=-N_c}^{N_c} \frac{1}{2i} (|n+1\rangle \langle n| - |n\rangle \langle n+1|). \end{aligned} \quad (\text{B1})$$

Additionally, for the estimation of the coherence times due to quasiparticle tunneling effects, we need to redefine the charge and the phase operator, where instead of representing number and tunneling of Cooper pairs, now it represents the number and tunneling of electrons $|n^{\text{SE}}\rangle$ [39]. In this representation, the relevant operators are expressed as follows

$$\begin{aligned} \hat{n} &= \sum_{n=-N_{E,c}}^{N_{E,c}} n^{\text{SE}} |n^{\text{SE}}\rangle \langle n^{\text{SE}}|, \\ \cos(\hat{\varphi}) &= \sum_{n=-N_{E,c}}^{N_{E,c}} \frac{1}{2} (|n^{\text{SE}}+2\rangle \langle n^{\text{SE}}| + |n^{\text{SE}}\rangle \langle n^{\text{SE}}+2|), \\ \sin(\hat{\varphi}) &= \sum_{n=-N_{E,c}}^{N_{E,c}} \frac{1}{2i} (|n^{\text{SE}}+2\rangle \langle n^{\text{SE}}| - |n^{\text{SE}}\rangle \langle n^{\text{SE}}+2|), \\ \cos\left(\frac{\hat{\varphi}}{2}\right) &= \sum_{n=-N_{E,c}}^{N_{E,c}} \frac{1}{2} (|n^{\text{SE}}+1\rangle \langle n^{\text{SE}}| + |n^{\text{SE}}\rangle \langle n^{\text{SE}}+1|), \\ \sin\left(\frac{\hat{\varphi}}{2}\right) &= \sum_{n=-N_{E,c}}^{N_{E,c}} \frac{1}{2i} (|n^{\text{SE}}+1\rangle \langle n^{\text{SE}}| - |n^{\text{SE}}\rangle \langle n^{\text{SE}}+1|). \end{aligned} \quad (\text{B2})$$

On the other hand, to obtain the numerical representation of the flux operator for modes represented in the charge basis, we obtained an expression relating the flux operator of the mode with all the charge operators of the device, computing the commutator [37]

$$\begin{aligned} \langle i | [\hat{\varphi}_m, \hat{H}] | j \rangle &= \omega_{ij} \langle i | \hat{\varphi}_m | j \rangle \\ &= \sum_k 8i [E_C]_{km} \langle i | \hat{n}_k | j \rangle \end{aligned} \quad (\text{B3})$$

For the implementation of operators representing *flux-like* modes, we made use of the harmonic oscillator basis, considering the linear part of each mode to construct the numerical representation of the operators by means of creation and annihilation operators such that

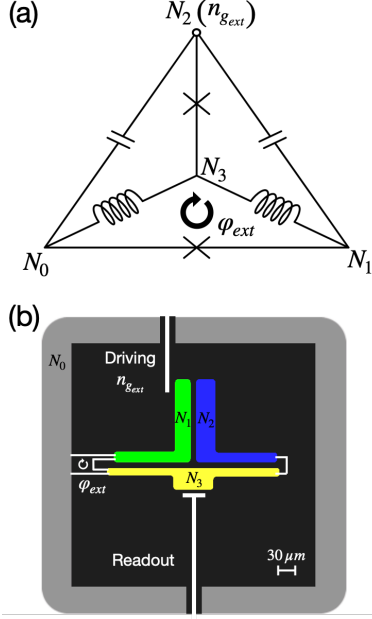


Figure 9: Proposed lithographic implementation for the optimized device. Lumped-element description of the device (top) followed by the geometric design (bottom) with indicated: nodes N_i , links between islands, driving and readout points. The colored part represents the optimized geometry, while the white parts act as schematics of branches and driving/readout structures.

$$\begin{aligned}\hat{n}_m &= \frac{i}{\sqrt{2}} \left(\frac{[E_L]_{mm}}{8[E_C]_{mm}} \right)^{\frac{1}{4}} (\hat{b}_m - \hat{b}_m^\dagger) \\ \hat{\varphi}_m &= \frac{1}{\sqrt{2}} \left(\frac{8[E_C]_{mm}}{[E_L]_{mm}} \right)^{\frac{1}{4}} (\hat{b}_m + \hat{b}_m^\dagger)\end{aligned}\quad (\text{B4})$$

In order to assure convergence of the numerical results, convergence test were conducted, leading to consider the cutoffs of $N_c = 20$ for charge-like modes and $N_f = 41$ for flux-like modes.

Appendix C: Lithographic Implementation

In the optimization process, special attention was put into evaluating designs in a range of physical parameters possible to implement in an experimental setup. As a proof of concept on the possibilities of fabrication of the device, here we propose a lithographic implementation of the system. The geometry was optimized using evolutionary optimization methods to best suit the capacitive relations

between circuit islands, still taking into consideration usual fabrication constraints. The procedure consisted of generating different parameterized geometrical layouts, which were optimized using evolutionary methods, numerically computing the capacitive relations between islands using a fast field solver [49, 50], and optimizing the parameters looking to match the capacitive relations of the theoretical design. For the evaluation of the degree of similarity between the theoretical and the lithographic design, the Frobenius norm of the matrix difference $\gamma = \sqrt{\sum_{ij} (C_{ij}^{\text{theo}} - C_{ij}^{\text{litho}})^2}$ was chosen. For simple geometrical designs, such as the one shown in Fig. 9, similarities of around $\gamma \approx 8.5$ fF were achieved, showing that the device expresses realistic capacitive relations for experimental setups.

Appendix D: Evolutionary algorithm

The problem of finding superconducting architectures expressing specific system characteristics can be described as a double optimization process over a discrete and continuous set. The algorithm must find suitable topologies by changing the arrangement (discrete) of the circuit component while finding the optimal circuit parameters (continuous) such that the device give rise to the targeted features. This problem is computational demanding because the discrete exploration need to be constructed such that it discards configurations with not available circuit Hamiltonian, i.e., we need to eliminate frozen and free terms corresponding to nodes where more than one inductor/capacitor are connected [51]. Another consideration relies on the exponential increasing of the Hilbert space with the number of nodes, which makes such exploration intractable by brute-force methods.

To tackle this problem, we use an evolutionary optimization approach. The algorithm was designed to converge to local solutions attaining the relevant features included in the cost function definitio \mathcal{F} . The evolutionary strategy used in this works relies on the proposed in [19]. The pseudocode is described in the Algorithm 1. The goal of the algorithm is to find a circuit topology \mathcal{T} and its correspondent component values $\mathcal{P}_{\mathcal{T}}$ that best match the requirements established by the cost function \mathcal{F} . The circuit structure considered for the optimization is the one depicted in Fig. 10, where we have established all-to-all connectivity between superconducting islands, assuming always a capacitive coupling, and either a linear and(or) nonlinear inductor connec-

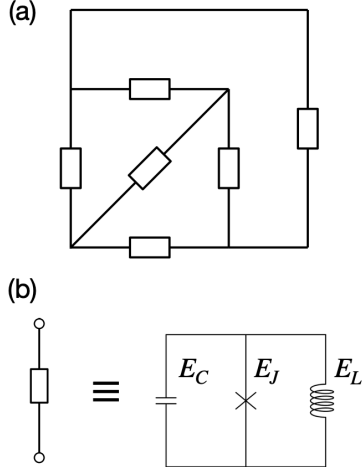


Figure 10: (a) Circuit structure considered of $N = 4$ superconducting islands with all-to-all connections where (b) each branch contains a capacitance and, depending on the configuration, a linear and(or) a non-linear inductor.

tion. The physical values of the circuit components were constrained to fabrication capabilities, to avoid unrealistic capacitive relations or extreme component values, complicating fabrication and reproducibility [52]. The optimization results were furthermore restricted to systems including three modes, discarding configurations expressing a lower number of modes. The recombination process was performed by properly combining suitable modes of the parent configurations, to obtain a resulting circuit with characteristics similar to the previous configurations. Mutations were performed over the circuit components and their physical values, by properly choosing the probability of mutation

p . The obtained solutions were observed not to represent global minima of the cost function but rather local solutions. While these solutions did not fully meet the cost function requirements, they showed resilience under small deviations in the continuous optimization parameters.

Algorithm 1 : Evolutionary circuit design

- 1: Define the circuit structure for optimization: number of superconducting islands N and connectivity
 - 2: Randomly create the initial population of M circuit instances with circuit configurations $\{\mathcal{T}, \mathcal{P}_{\mathcal{T}}\}$
 - 3: **for** n in generation **do**
 - 4: calculate the fitness \mathcal{F} of each individual by constructing and numerically diagonalizing the Hamiltonian describing the circuit
 - 5: choose the $M - p$ individual with the highest fitness
 - 6: **crossover:**
 - 7: **for** i in $M - p$ **do**
 - 8: randomly select two circuits from $M - p$
 - 9: recombine them to generate a new circuit
 - 10: **if** recombined circuit is a valid configuration **then**
 - 11: save it as an offspring
 - 12: **else**
 - 13: repeat
 - 14: **end if**
 - 15: **end for**
 - 16: **mutation:**
 - 17: **if** random number $\leq p$ **then**
 - 18: change a circuit instance by modifying its topology or varying its components values
 - 19: **end if**
 - 20: $Initial\ population \leftarrow the\ offsprings$
 - 21: **end for**
 - 22: Fine-tune the circuit parameters for the architecture chosen by means of gradient descend optimization
-

[1] V. Bouchiat, D. Vion, P. Joyez, D. Esteve, and M. H. Devoret, *Physica Scripta* **1998**, 165 (1998).
 [2] Y. Nakamura, Yu. A. Pashkin, and J. S. Tsai, *Nature* **398**, 786-788 (1999).
 [3] J. E. Mooij, T. P. Orlando, L. Levitov, L. Tian, C. H. Van der Wall, and S. Lloyd, *Science* **285**, 5430 (1999).
 [4] J. Koch, T. M. Yu, J. Gambetta, A. A. Houck, D. I. Schuster, J. Majer, A. Blais, M. H. Devoret, S. M. Girvin and R. J. Schoelkopf, *Physical Review A* **76**, 042319 (2007).
 [5] V. E. Manucharyan, J. Koch, L. I. Glazman, and M. H. Devoret, *Science* **326**, 5949 (2009).
 [6] A. P. M. Place, L. V. H. Rodgers, P. Mundada, B. M.

Smitham, M. Fitzpatrick, Z. Leng, A. Premkumar, J. Bryon, A. Vrajitoarea, S. Sussman, G. Cheng, T. Madhavan, H. K. Babla, X. H. Le, Y. Gang, B. Jäck, A. Gyenis, N. Yao, R. J. Cava, N. P. de Leon, and A. A. Houck, *Nature Communications* **12** 1779 (2021).
 [7] C. Wang, X. Li, H. Xu, Z. Li, J. Wang, Z. Yang, Z. Mi, X. Liang, T. Su, C. Yang, G. Wang, W. Wang, Y. Li, M. Chen, C. Li, K. Linghu, J. Han, Y. Zhang, Y. Feng, Y. Song, T. Ma, J. Zhang, R. Wang, P. Zhao, W. Liu, G. Xue, Y. Jin, and H. Yu, *npj Quantum Information* **8**, 3 (2022).
 [8] A. Somoroff, Q. Ficheux, R. A. Mencia, H. Xiong, R. Kuzmin, and V. E. Manucharyan, *Physical Review Letters* **130**, 267001 (2023).

- [9] A. Gyenis, A. Di Paolo, J. Koch, A. Blais, A. A. Houck, and D. I. Schuster, *PRX Quantum* **2**, 030101 (2021).
- [10] A. Calzona, and M. Carrega, *Superconductor Science and Technology* **36** 023001 (2023).
- [11] L. B. Ioffe, M. V. Feigel'man, A. Ioselevich, D. Ivanov, M. Troyer, and G. Blatter, *Nature* **415** 503-506 (2002).
- [12] S. Gladchenko, D. Olaya, E. Dupont-Ferrier, B. Douçot, L. B. Ioffe, and M. E. Gershenson, *Nature* **5** 48-53 (2009).
- [13] B. Douçot, and L. B. Ioffe, *Reports on Progress in Physics* **75** 072001 (2012).
- [14] P. Brooks, A. Kitaev, and J. Preskill, *Physical Review A* **87** 052306 (2013).
- [15] W. C. Smith, A. Kou, X. Xiao, U. Vool, and M. H. Devoret, *npj Quantum Information* **6** 8 (2020).
- [16] K. Kalashnikov, W. T. Hsieh, W. Zhang, W. Lu, P. Kamenov, A. Di Paolo, A. Blais, M. E. Gershenson, and M. Bell, *PRX Quantum* **1** 010307 (2020).
- [17] E. Hyppä, S. Kundu, C. F. Chan, A. Gunyhó, J. Hotari, D. Janzso, K. Juliusson, O. Kiuru, J. Kotilahti, A. Landra, W. Liu, F. Marxer, A. Mäkinen, J. Orgiazzi, M. Palma, M. Savytskyi, F. Tosto, J. Tuorila, V. Vadimov, T. Li, C. Ockeloen-Korppi, J. Heinsoo, K. Y. Tan, J. Hassel, and M. Möttönen, *Nature Communications* **13** 6895 (2022).
- [18] R. A. Mencia, W. Lin, H. Cho, M. G. Vavilov, and V. E. Manucharyan, *arXiv:2403.16780* (2024).
- [19] F. A. Cárdenas-López, J. C. Retamal, X. Chen, G. Romero, and M. Sanz, *arXiv:2302.01837* (2023).
- [20] A. J. Leggett, S. Chakravarty, A. T. Dorsey, M. P. A. Fisher, A. Garg, and W. Zwerger, *Reviews of Modern Physics* **67** 725 (1987).
- [21] P. Groszkowski, A. Di Paolo, A. L. Grimsmo, A. Blais, D. I. Schuster, A. A. Houck and J. Koch, *New Journal of Physics* **20** 043053 (2018).
- [22] P. Groszkowski, and J. Koch, *Quantum* **5** 583 (2021).
- [23] G. Ithier, E. Collin, P. Joyez, P. J. Meeson, D. Vion, D. Esteve, F. Chiarello, A. Shnirman, Y. Makhlin, J. Schrieffer, and G. Schön, *Physical Review B* **72** 134519 (2005).
- [24] D. M. Pozar, *Microwave Engineering*. 4th Edition (Wiley, New York, 2012).
- [25] P. Krantz, M. Kjaergaard, F. Yan, T. P. Orlando, S. Gustavsson, and W. D. Oliver, *Applied Physics Review* **6** 021318 (2019).
- [26] I. M. Pop, K. Geerlings, G. Catelani, R. J. Schoelkopf, L. I. Glazman, and M. H. Devoret, *Nature* **508**, 369 (2014).
- [27] L. B. Nguyen, Y. Lin, A. Somoroff, R. Mencia, N. Grabon, and V. E. Manucharyan, *Physical Review X* **9** 041041 (2019).
- [28] P. van Mulbregt, and SciPy 1.0 Contributors. *SciPy 1.0: Fundamental Algorithms for Scientific Computing in Python*. *Nature Methods*, **17**, 261 (2020).
- [29] A. Blais, R.-S. Huang, A. Wallraff, S. M. Girvin, and R. J. Schoelkopf, *Physical Review A* **69**, 062320 (2004).
- [30] R. Bianchetti, S. Filipp, M. Baur, J. M. Fink, C. Lang, L. Steffen, M. Boissonneault, A. Blais, and A. Wallraff, *Physical Review Letters* **105**, 223601 (2010).
- [31] E. A. Sete, J. M. Martinis, and A. N. Korotkov, *Phys. Rev. A* **92**, 012325 (2015).
- [32] R. Shillito, A. Petrescu, J. Cohen, J. Beall, M. Hauru, M. Ganahl, A. G. M. Lewis, G. Vidal, and A. Blais, *Phys. Rev. Applied* **18**, 034031 (2022).
- [33] M. Boissonneault, J. M. Gambetta, and A. Blais, *Physical Review A* **77**, (060305)(R).
- [34] F. Motzoi, L. Buchmann, C. Dickel, *arXiv:1809.04116 [quant-ph]* (2018).
- [35] G. Catelani, R. J. Schoelkopf, M. H. Devoret and L. I. Glazman, *Physical Review B* **84**, 064517 (2011).
- [36] J. Koch, V. Manucharyan, M. H. Devoret and L. I. Glazman, *Physical Review Letters* **103**, 217004 (2009).
- [37] H. Zhang, S. Chakram, T. Roy, N. Earnest, Y. Lu, Z. Huang, D. K. Weiss, J. Koch, and D. I. Schuster, *Physical Review X* **11**, 011010 (2021).
- [38] L. B. Nguyen, G. Koolstra, Y. Kim, A. Morvan, T. Chistolini, S. Singh, K. N. Nesterov, C. Jünger, L. Chen, Z. Pedramrazi, B. K. Mitchell, J. M. Kreikebaum, S. Puri, D. I. Santiago and I. Siddiqi, *PRX Quantum* **3**, 037001 (2022).
- [39] G. Catelani, R. J. Schoelkopf, M. H. Devoret and L. I. Glazman, *Physical Review B* **84**, 064517 (2011).
- [40] A. Gyenis, P. S. Mundada, A. Di Paolo, T. M. Hazard, X. You, D. I. Schuster, J. Koch, A. Blais and A. A. Houck, *PRX Quantum* **2**, 010339 (2021).
- [41] A Kou, W. C. Smith, U. Vool, R. T. Brierley, H. Meier, L. Frunzio, S. M. Girvin, L. I. Glazman and M. H. Devoret, *Physical Review X* **7** 031037 (2017).
- [42] F. Yoshihara, K. Harrabi, A. O. Niskanen, Y. Nakamura and J. S. Tsai, *Physical Review Letters* **97**, 167001 (2006).
- [43] L. H. Pedersen, N. M. Møller, and K. Mølmer, *Physics Letters A* **367**, 47 (2007).
- [44] F. Motzoi, J. M. Gambetta, P. Rebentrost, and F. K. Wilhelm, *Physical Review Letters* **103**, 110501 (2009).
- [45] Z. Chen, et al., *Physical Review Letters*, **116**, 020501 (2016).
- [46] J. M. Martinis and M. R. Geller, *Physical Review A* **90**, 022307 (2014).
- [47] F. Motzoi and F. K. Wilhelm, *Physical Review A* **88**, 062318 (2013).
- [48] F. Pfeiffer, et al., *arXiv:2312.16988 [quant-ph]* (2023).
- [49] S. R. L, *FastFieldSolvers*. Fast Field Solvers products.
- [50] K. Nabors, and J. White. *IEEE Transactions on Computer-Aided Design of Integrated Circuits and Systems*, **10**, 1447 (1991).
- [51] S. P. Chitta, T. Zhao, Z. Huang, I. Mondragon-Shem, J. Koch, *New J. Phys.* **24** 103020 (2022).
- [52] G. Wedin, *Rep. Prog. Phys.* **80**, 106001 (2017).